

<https://doi.org/10.1038/s44310-026-00122-8>

Single-shot full-Stokes polarization and quantitative phase imaging via a single-layer metalens

Check for updates

Qiangbo Zhang¹, Peicheng Lin², Xinyuan Jiang¹, Linze Li³, Jiaming Liang³, Huai Xia¹, Changwei Zhang¹, Chang Wang¹, Chenying Yang³, Yubing Han¹, Ting Xu²✉ & Zhenrong Zheng¹✉

Conventional image sensors are intrinsically limited to detecting optical intensity, thereby missing the rich phase and polarization dimensions of the light field. While characterizing these parameters is essential for understanding the intrinsic properties of objects, current multidimensional imaging techniques are often plagued by bulky optical setups, time-sequential scanning, or coherent noise artifacts. Here, we present a compact, single-shot imaging strategy capable of simultaneously retrieving full-Stokes polarization and quantitative phase information using a single-layer metalens. Our design utilizes the metalens to project the incident light onto distinct regions of a polarization camera. By introducing a predefined focal shift between isotropic sub-regions, we enable motion-free phase retrieval via the transport-of-intensity equation, while simultaneously separating chiral polarization states to reconstruct the complete Stokes vector. Using speckle-suppressed LED illumination, we experimentally demonstrate simultaneous full-Stokes polarization and quantitative phase imaging. This miniaturized architecture may pave the way for portable, real-time multidimensional optical sensing platforms.

Optical fields are characterized by multidimensional properties, primarily intensity, phase, and polarization. Phase information reveals the optical thickness and refractive index distribution of objects, which is critical for inspecting transparent biological samples and optical components¹. Polarization information, conversely, discloses surface morphology² and chiral features³. However, standard commercial image sensors typically respond only to light intensity, discarding phase and polarization data. Consequently, developing techniques capable of efficiently acquiring these multidimensional parameters is essential for applications in biomedical imaging^{1,4}, material characterization⁵, and remote sensing⁶.

While traditional quantitative phase imaging (QPI) and polarimetry are well-established, they are often hindered by system complexity, bulkiness, and low temporal resolution. For instance, regarding phase retrieval, classical interferometry offers high precision but requires stringent environmental stability and a separate reference arm^{7–9}. Although self-referenced common-path techniques, such as cyclic shearing^{10,11}, alleviate these stability constraints, they still require nontrivial optical configurations. Similarly, the transport-of-intensity equation (TIE), a non-interferometric phase retrieval approach, generally requires mechanical axial scanning to capture through-focus intensity stacks, precluding its use in dynamic scenarios^{12–14}. In the

realm of polarization, conventional methods typically rely on sequential modulation of rotating polarizers or waveplates to reconstruct full Stokes vectors, making snapshot acquisition not straightforward¹⁵. To address this limitation, computational imaging approaches, including compressive reconstruction and learning-based methods, have recently emerged as promising routes toward single-shot full-Stokes polarimetry^{16,17}. Despite these individual advancements, realizing simultaneous single-shot full-Stokes polarization and quantitative phase imaging within a compact form factor remains a persistent challenge.

Metasurfaces—planar optical elements composed of subwavelength scatterers—have provided a transformative solution by enabling precise control over light amplitude, phase, and polarization, offering new avenues to overcome the limitations of conventional optics^{18–30}. Consequently, compact metasurface-based imaging systems have attracted significant interest. For example, polarization-multiplexed metalenses have been designed to achieve single-shot TIE phase imaging^{31–37}, while metasurface-based polarization cameras have enabled instantaneous full-Stokes imaging^{38–43}. These advances demonstrate the substantial potential of metasurfaces for integrated, multidimensional optical field sensing.

¹College of Optical Science and Engineering, Zhejiang University, Hangzhou, China. ²National Laboratory of Solid-State Microstructures, Collaborative Innovation Center of Advanced Microstructures, College of Engineering and Applied Sciences, Nanjing University, Nanjing, China. ³Hangzhou Institute for Advanced Study, University of Chinese Academy of Sciences, Hangzhou, China. ✉e-mail: xuting@nju.edu.cn; zrz@zju.edu.cn

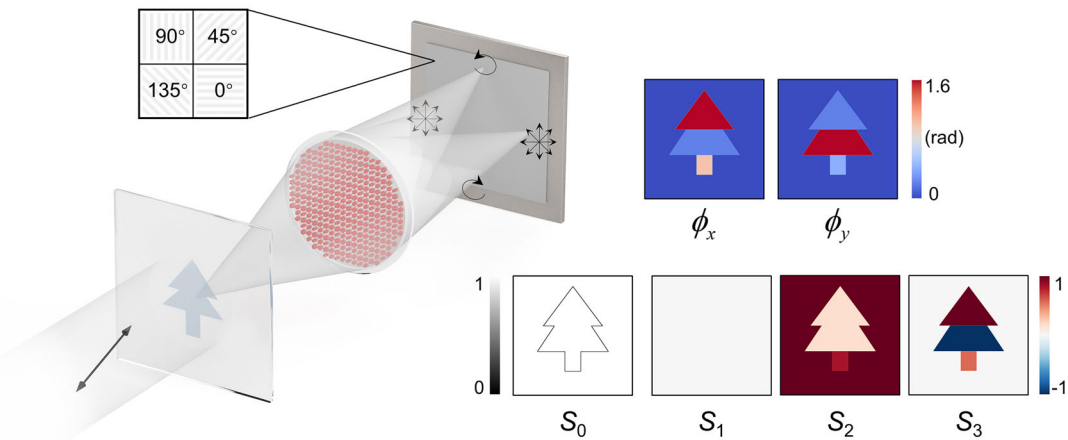


Fig. 1 | Schematic of the metalens-assisted snapshot full-Stokes polarization and quantitative phase imaging system. The metalens images the scene information onto four distinct regions of a polarization camera. Based on the captured intensity

images, both the phase distribution and the full-Stokes parameters of the scene can be reconstructed.

Despite this progress, current metasurface-based imaging platforms face inherent limitations. Most existing designs prioritize the retrieval of a single optical dimension, failing to simultaneously achieve high-fidelity full-Stokes polarization and quantitative phase imaging within a compact architecture. While recent efforts have attempted to combine these modalities⁴⁴, they predominantly rely on coherent laser sources. This reliance inevitably introduces speckle noise, degrading the signal-to-noise ratio. Therefore, achieving single-shot full-Stokes polarization and quantitative phase imaging within a compact framework under speckle-suppressed illumination remains a critical unresolved issue.

In this work, we propose a single-shot full-Stokes polarization and quantitative phase imaging method enabled by a meta-unit-encoded metalens. We utilize a novel “four-in-one” meta-unit as the fundamental building block to spatially multiplex scene information onto four distinct regions of a polarization sensor. To satisfy the TIE requirement for focused and defocused images, we engineer a slight physical focal length difference between the left and right imaging regions using isotropic nanopillars, thereby eliminating the need for mechanical motion. Simultaneously, anisotropic nanopillars serve to spatially separate left- and right-handed circular polarizations. By combining these circularly polarized components with the detector’s intrinsic linear-polarization channels, the system facilitates the reconstruction of the complete Stokes vector. Crucially, our design is compatible with partially coherent illumination, enabling speckle-suppressed imaging using a narrowband-filtered LED source. We experimentally demonstrate the system’s capability through full-parameter imaging of anisotropic metasurfaces and dynamic phase imaging of living cells, establishing its potential for compact, multidimensional optical sensing.

Results

Metalens design and system overview

Figure 1 illustrates the schematic diagram of our metalens-assist snapshot full-Stokes polarization and quantitative phase imaging system. We employ a meta-unit-encoded metalens to selectively image scene information onto four distinct regions of a polarization sensor. By processing these four sub-images, the complete decoding of the intensity, phase, and polarization information of the scene can be achieved. Specifically, we adopt the four-in-one meta-unit shown in Fig. 2b as the fundamental building block of the metalens, with each substructure detailed in Fig. 2a. Among them, substructures 1 and 4 are isotropic nanopillars—with equal length and width and no in-plane rotation—which image scene information onto the left and right sub-regions of the polarization sensor without polarization selectivity. These two channels are intentionally designed with slightly different focal lengths, allowing us to decode the phase distributions corresponding to

different polarization states by applying the TIE. In contrast, substructures 2 and 3 are anisotropic nanopillars, which selectively focus left-circularly polarized (LCP) and right-circularly polarized (RCP) light onto the upper and lower sub-regions, respectively, providing the necessary chirality information for decoding the full Stokes parameters. Simultaneous separation of both LCP and RCP components helps mitigate polarization mixing in the recorded intensities, facilitating the subsequent joint reconstruction of polarization and phase information.

We define four different phase distributions of the metalens for the four sub-images captured by the polarization sensor as follows:

$$\varphi_{\text{Left}} = -\frac{2\pi}{\lambda} \times \left(\sqrt{(x+D)^2 + y^2 + f_1^2} - \sqrt{D^2 + f_1^2} \right), \quad (1)$$

$$\varphi_{\text{Right}} = -\frac{2\pi}{\lambda} \times \left(\sqrt{(x-D)^2 + y^2 + f_2^2} - \sqrt{D^2 + f_2^2} \right), \quad (2)$$

$$\varphi_{\text{Up/Down}} = -\frac{2\pi}{\lambda} \times \left(\sqrt{x^2 + (y \mp D)^2 + f_1^2} - \sqrt{D^2 + f_1^2} \right). \quad (3)$$

Here, $\lambda = 780 \text{ nm}$, (x, y) denote coordinates on the metalens, focal lengths f_1 and f_2 are set at 12.5 mm and 12 mm respectively, and offset $D = 1 \text{ mm}$. φ_{Left} and φ_{Right} are realized using isotropic nanopillars (substructures 1 and 4), while φ_{Up} and φ_{Down} utilize anisotropic nanopillars (substructures 2 and 3). Specifically, the propagation phase η and geometric phase ψ for anisotropic nanopillars follow $\eta = (\varphi_{\text{Up}} + \varphi_{\text{Down}})/2$, $\psi = (\varphi_{\text{Up}} - \varphi_{\text{Down}})/2$. We choose amorphous silicon (a-Si) as the material for these meta-units, with a period of 350 nm and a nanopillar height of 400 nm. The parameters of the selected isotropic nanopillars, along with their transmission efficiencies and achievable phase shifts, are shown in Fig. 2c. The comprehensive parameter database allows us to achieve nearly any desired phase shift within a full 2π range. By mapping the polarization conversion efficiencies (Fig. 2d) and the propagation phase shifts (Fig. 2e) against the structural parameters, we select 16 anisotropic nanopillars capable of achieving polarization conversion efficiencies above 90% and covering a full 2π propagation phase range (Fig. 2f). The required geometric phases ψ for anisotropic nanopillars are achieved by rotating these nanopillars by appropriate angles.

Due to the slight focal-length difference designed between φ_{Left} and φ_{Right} , we can solve the phase distribution using the TIE from the left and right sub-images. For monochromatic paraxial light propagation, the phase

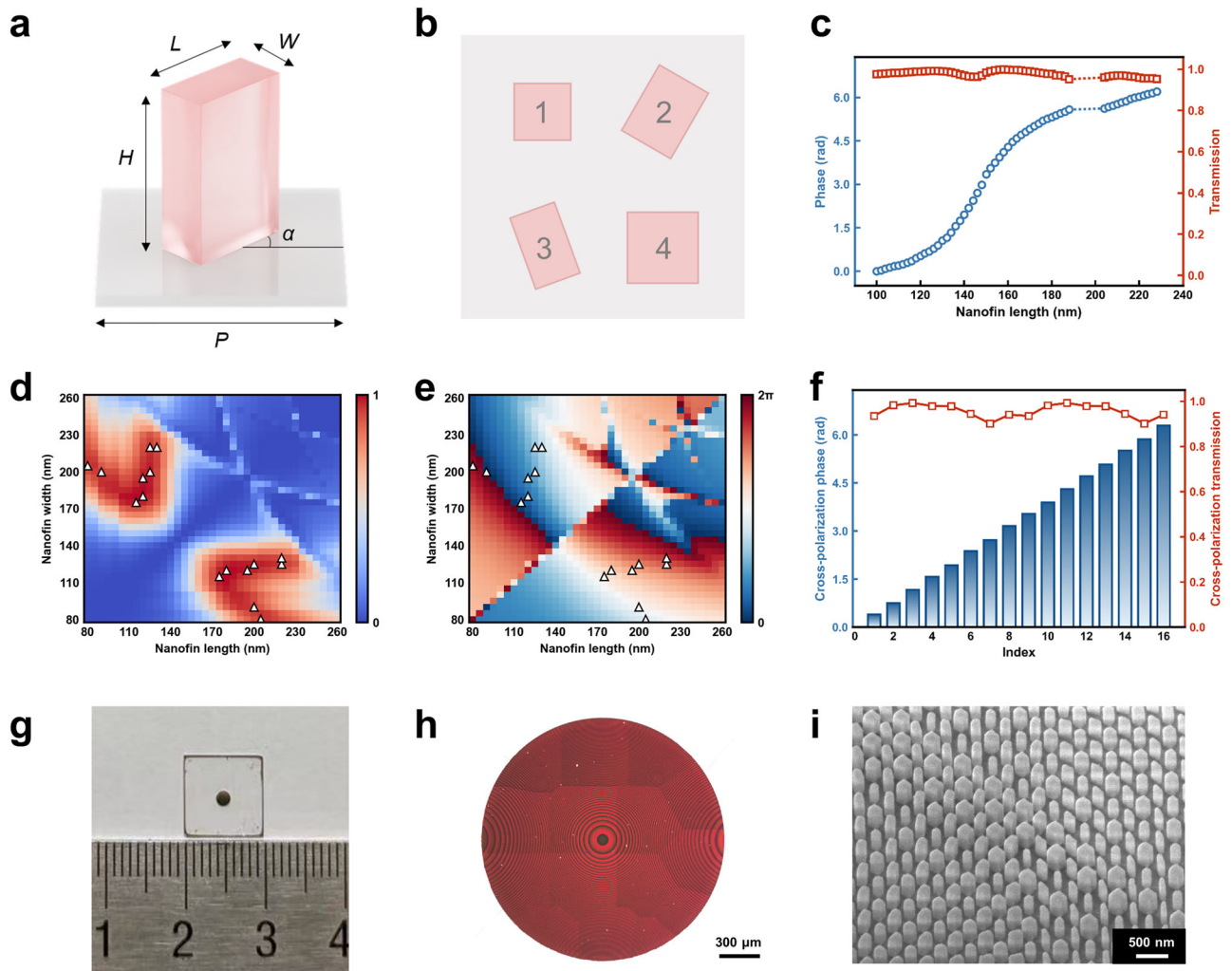


Fig. 2 | Design and fabricated sample of the metalens. **a** Schematic of the sub-unit cell within the meta-unit, consisting of an amorphous silicon nanofin on a silica substrate. The period P is 350 nm and the nanofin height H is 400 nm. The operational wavelength is designed to be 780 nm. **b** Schematic of the four-in-one meta-unit structure, in which elements 1 and 4 are isotropic nanofins and elements 2 and 3 are anisotropic nanofins. **c** Transmission and phase shifts of selected isotropic nanofins versus side length. **d** Mapping of cross-polarized transmission and (e)

phase shifts for anisotropic nanofins versus their length and width. Triangular markers denote the selected nanofin designs. **f** Cross-polarized transmission and phase shifts corresponding to the selected anisotropic nanopillars in (d) and (e). **g** Photograph of the fabricated 1.8-mm-diameter metalens. **h** Optical microscopy image of the fabricated metalens. **i** Scanning electron microscope image of the fabricated metalens.

distribution $\phi(x, y)$ can be solved using the TIE¹²:

$$\phi(x, y) = -k\nabla^{-2}\nabla \cdot \left[I^{-1}(x, y)\nabla\nabla^{-2}\frac{\partial I(x, y)}{\partial z} \right], \quad (4)$$

where k is the wave number, $I(x, y)$ denotes the in-focus intensity at the left sub-region of the sensor, ∇ represents the transverse gradient operator with respect to coordinates (x, y) , and z is the axial propagation coordinate. Since the left and right sub-images are formed through isotropic nanopillars without altering the polarization state, we can recover the phase distributions at 0° and 90° polarization states simultaneously when combined with a polarization sensor. However, as the two phase distributions are retrieved independently, they may exhibit a constant offset, which prevents direct full-Stokes parameters reconstruction. Therefore, additional polarization channels corresponding to LCP and RCP light are required, as provided by substructures 2 and 3 of the meta-unit. By combining the four linearly polarized measurements from the left polarization sensor region with the circularly polarized measurements from the upper and lower regions, we can reconstruct the complete Stokes vector of the scene. Thus, our

method enables full retrieval of the scene's intensity, phase, and polarization information.

To experimentally validate our design, we fabricated a 1.8-mm-diameter metalens, as shown in Fig. 2g. The corresponding optical microscope image is presented in Fig. 2h, where stitching marks were introduced during the electron-beam lithography (EBL) process. The scanning electron microscope (SEM) image in Fig. 2i clearly reveals the interleaved four-in-one meta-unit arrangement.

Full-Stokes polarization reconstruction

We evaluated the full-Stokes polarization reconstruction capability of our metalens system using the optical configuration shown in Fig. 3a. Collimated light from an LED source (Thorlabs, M780L3-C1) sequentially passed through a 780 nm narrowband filter (Thorlabs, FBH780-10), a linear polarizer (LP), and a quarter-wave plate (QWP), and was then incident on a 300 μm -diameter pinhole. The metalens subsequently imaged the pinhole onto four sub-regions of the polarization sensor (Sony IMX264). The sensor features a resolution of 2448 \times 2048 with a pixel size of 3.45 μm .

As a representative example, Fig. 3b shows the four linear polarization images captured by the polarization sensor under 90° linearly polarized

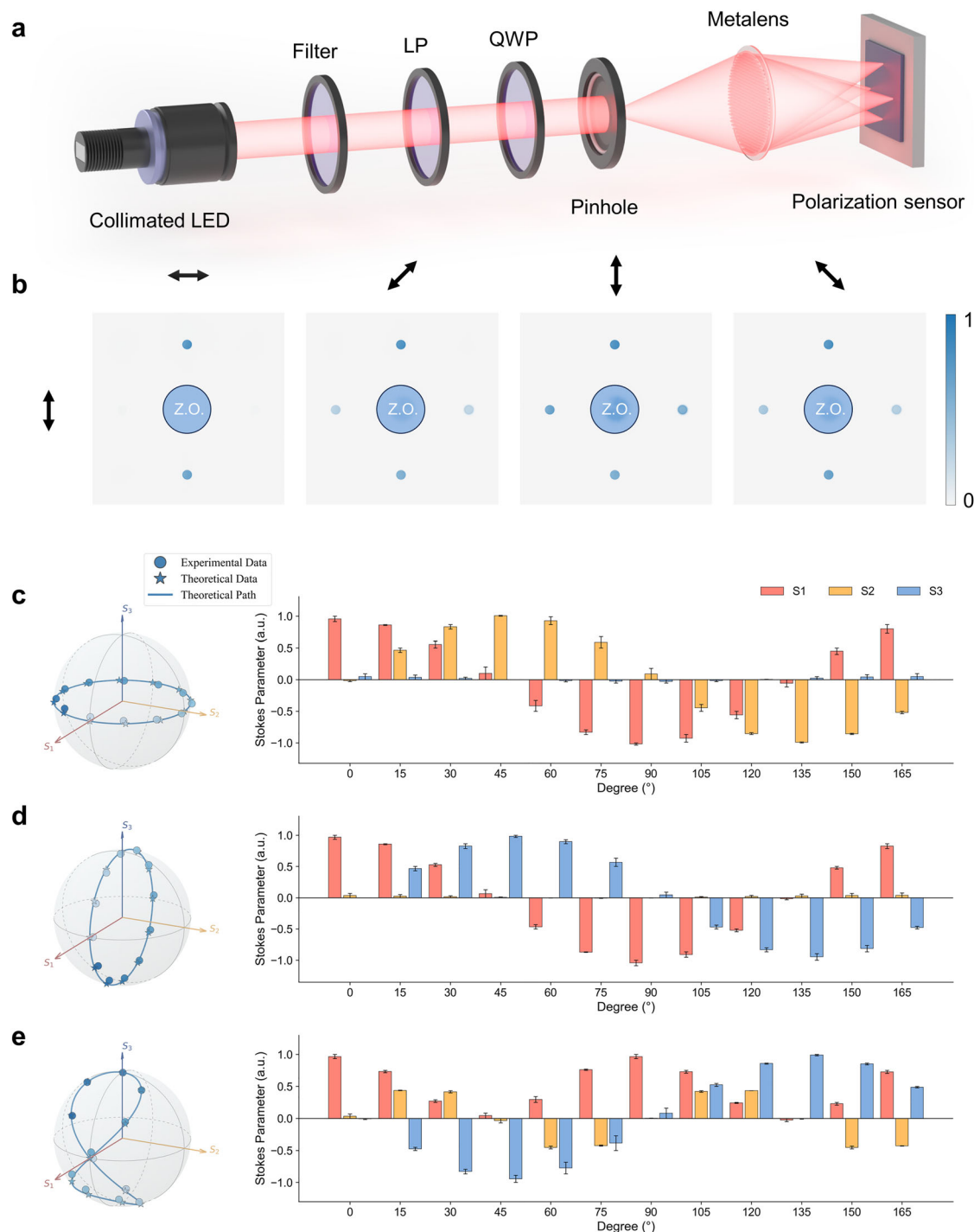


Fig. 3 | Full-Stokes polarimetric measurements. **a** Optical setup for full-Stokes polarimetric reconstruction using the metalens. **b** Four polarization images captured by the polarization sensor under 90° linearly polarized illumination. **c–e** Reconstructed Stokes parameters (S_1 , S_2 , S_3) and corresponding points on the Poincaré

sphere for three types of input polarization modulation: (c) rotating the linear polarizer (LP) alone; (d) rotating the LP with the quarter-wave plate (QWP) fast axis fixed at 0°; (e) rotating the QWP with the LP fixed at 0°. Error bars represent deviations between the reconstructed and theoretical Stokes parameters.

illumination. In the 0° polarization channel, only the upper and lower regions corresponding to circular polarization exhibit signal, while the isotropic regions on the left and right remain dark. This occurs because the isotropic nanopillars direct light to the left and right regions without modifying its polarization state, which is blocked by the 0° analyzer. When the sensor channel is set to 45° or 135°, the circular regions remain nearly unchanged, whereas the isotropic regions appear brighter, reaching maximum intensity at 90°. These observations agree well with the designed polarization-dependent response of the metalens.

We next performed quantitative reconstruction of the Stokes polarization parameters. Given that the polarization sensor may exhibit inter-channel crosstalk, system calibration was first carried out (see Supplementary Information for details). Then we tested three polarization modulation schemes: rotating the LP alone, (ii) rotating the LP with the QWP fast axis fixed at 0°, and (iii) rotating the QWP with the LP fixed at 0°. The reconstructed Stokes parameters (S_1 , S_2 , S_3) for these three cases are shown in Fig. 3c–e, along with their deviations from theoretical values and their respective locations on the Poincaré sphere. The reconstructed points

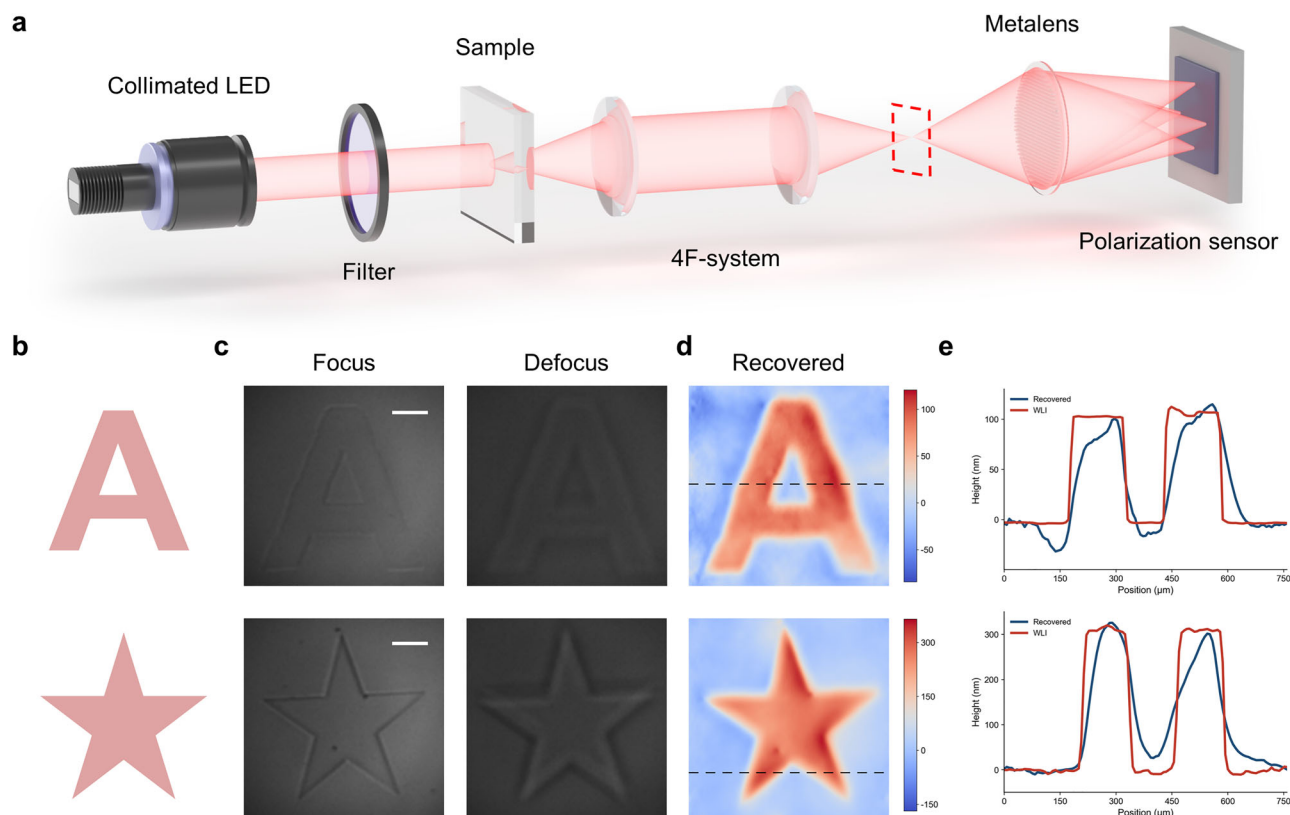


Fig. 4 | Phase measurement. **a** Optical setup for testing the artificial phase objects. **b** Pattern of the artificial phase objects. **c** Captured intensity images at the in-focus and defocused planes. Scale bars: 150 μm . **d** Recovered thickness map of the objects. **e** Thickness profiles along the black dashed lines in **(d)**, overlaid with the corresponding white-light interferometer (WLI) measurements.

closely follow the theoretical trajectories and are well aligned with the expected positions on the Poincaré sphere. The average reconstruction errors for the three input cases are 7.4×10^{-2} , 4.4×10^{-2} , and 4.5×10^{-2} rad, respectively. These results demonstrate the high-fidelity performance of our metalens-assisted system in full-Stokes polarization reconstruction.

Quantitative phase imaging validation

To validate the quantitative phase recovery capability of our metalens-assisted imaging system, we constructed the optical setup shown in Fig. 4a. A collimated LED beam passed through a 780 nm narrowband filter (10 nm FWHM) and illuminated the sample; the illumination is partially coherent, so an effective wavelength is used in the TIE reconstruction and spectral averaging is negligible. A 4 f relay system then formed a real intermediate image, as indicated by the red dashed region, where an iris was inserted to limit the image size. This intermediate image was subsequently focused by the metalens onto four sub-regions of the polarization camera. Two artificial phase targets with varying thicknesses were fabricated using silica (SiO_2) as test samples, as illustrated in Fig. 4b. The corresponding in-focus and defocused intensity images, acquired under the 90° linear polarization channel of the sensor, are shown in Fig. 4c (from the left and right sub-regions, respectively). The acquired intensity pairs were processed using a TIE-based algorithm (see Supplementary Information) to recover the phase distribution. To ensure reconstruction accuracy, we applied frequency-domain scaling to correct magnification discrepancies (Fig. S1) and performed background phase calibration to eliminate systematic artifacts (Fig. S2). The recovered phase was then converted into thickness maps by

$$z(x, y) = \frac{\lambda \cdot \varphi(x, y)}{2\pi \cdot \Delta n}, \quad (5)$$

where Δn is the refractive index difference between SiO_2 and air. The reconstructed thickness maps are shown in Fig. 4d. Cross-sectional thickness profiles extracted along the black dashed lines are plotted in Fig. 4e, together with the corresponding white-light interferometer (WLI) measurements acquired along the same line cuts. The agreement between the reconstructed and WLI-measured profiles demonstrates the effectiveness of our metalens-assisted system for quantitative phase reconstruction. The spatial resolution of the imaging system was further characterized using a 1951 USAF resolution target, as shown in Fig. S3.

Multidimensional imaging results

We fabricated a single anisotropic metasurface sample ($400 \times 400 \mu\text{m}^2$), composed of a periodic array of identical rectangular nanopillars with unequal length and width (Fig. S4), as a representative target for multidimensional imaging. Using the setup in Fig. 4a and 45° linearly polarized illumination, we captured the corresponding intensity and reconstructed phase (90° polarization channel; applicable throughout Fig. 5), shown in the first two panels of Fig. 5a (see Fig. S5 for the recorded 4-pol images). We note that the dark boundary features introduced during fabrication may have impacted the accuracy of the reconstructed phase. The last two panels in Fig. 5a show the reconstructed degree of linear polarization (DoLP) and degree of circular polarization (DoCP), with $\text{DoLP} = \frac{\sqrt{S_1^2 + S_2^2}}{S_0}$ and $\text{DoCP} = \frac{S_3}{S_0}$. The observed polarization characteristics are generally consistent with the anisotropic metasurface design.

We also implemented the metalens-assisted system in a microscopic imaging configuration (Fig. S6). Figure 5b presents the reconstructed intensity, phase, and polarization images of a single U2OS cell. While the system demonstrates effective phase imaging performance, the polarization response appears weak. This limited contrast may arise from spatial

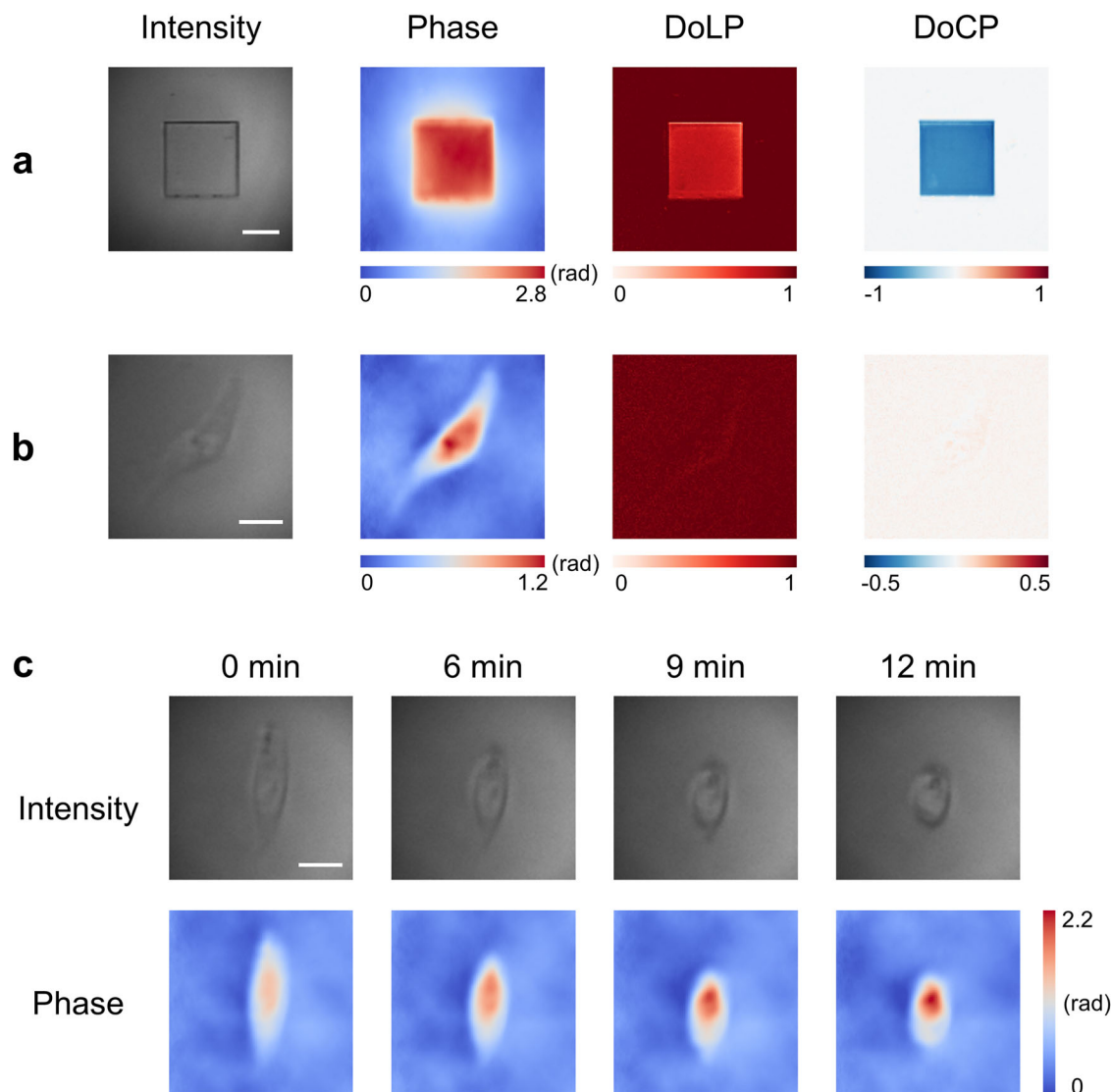


Fig. 5 | Intensity, phase, and polarization results of different samples, as well as dynamic phase retrieval of live cells. Reconstructed intensity, phase, and polarization images of (a) an anisotropic metasurface sample and (b) a single U2OS cell.

c Dynamic intensity and phase imaging of a U2OS cell treated with a 0.0125% trypsin-EDTA solution. Scale bars: 200 μm (a) and 20 μm (b, c).

averaging within the finite resolution volume, where sub-micron cytoskeletal birefringence is diluted by the background and partially offset by local orientation heterogeneity⁴⁵.

The single-shot nature of our system enables the observation of live-cell morphological dynamics. Figure 5c presents time-lapse intensity and corresponding quantitative phase images of a single U2OS cell treated with a 0.0125% trypsin-EDTA solution to induce cell detachment. Over a span of 12 min, the cell rapidly contracts from a spread morphology to a spherical shape, accompanied by a significant increase in the central phase delay. These results demonstrate the capability of our system to perform real-time, label-free, and dynamic monitoring of live-cell morphological evolution.

Discussion

As with many TIE-based approaches, the proposed phase retrieval method is most suitable for weakly absorbing objects with smoothly varying phase. For targets with strong absorption or pronounced intensity contrast, the TIE assumptions may be less well satisfied, which can introduce bias in the recovered phase. This limitation primarily affects the phase reconstruction, while snapshot full-Stokes polarization imaging can still be performed.

In conclusion, we present a snapshot full-Stokes polarization and quantitative phase imaging system that integrates a single-layer metasurface with a polarization-sensitive sensor, enabling simultaneous full-Stokes vector retrieval and quantitative phase reconstruction under partially coherent LED illumination. The metalens employs an interleaved four-in-one meta-unit design to achieve compact, integrated polarization multiplexing while eliminating the need for mechanical scanning or external optics. Although our design is applicable to coherent frameworks, we employed a narrowband-filtered LED source to suppress speckle noise and interference artifacts, ensuring high signal-to-noise ratio for robust phase and polarization retrieval.

Through both anisotropic metasurface samples and live-cell imaging experiments, we demonstrated the system's capability in polarization characterization of anisotropic metasurfaces and label-free monitoring of cellular morphology. Our work provides a practical and scalable approach for real-time, label-free, multidimensional optical imaging, with potential applications in microstructure characterization, live-cell dynamics, and biomedical diagnostics. Furthermore, integration with deep learning holds promise for enabling intelligent feature extraction, enhancing phase reconstruction, and facilitating multidimensional data fusion.

Methods

Metasurface fabrication

The process begins with plasma enhanced chemical vapor deposition of an a-Si film on a 500- μm -thick fused silica substrate, the thicknesses of a-Si is 400 nm for the metalens and 630 nm for the anisotropic metasurface sample. After oxygen plasma cleaning, a layer of hexamethyldisilazane is vapor-coated on the a-Si film to enhance adhesion. After spin-coating a layer of 200-nm-thick positive E-beam resist, a thin layer of water-soluble E-spacer is applied to mitigate the charging effect during later exposure. Next, the nanopattern is defined in the resist by using E-beam lithography, followed by development in o-Xylene. The 30-nm-thick aluminum as hard mask with reversed pattern is obtained via an E-beam evaporator and a gentle lift-off process in n-methyl-pyrrolidone. Inductively coupled plasma reactive ion etching with an optimized recipe is implemented to introduce the pattern into a-Si, where the chamber pressure is 10 mTorr, the flow ratio of C4F8/SF6 is 1.1, the RF power of ICP generator is 2000 W, the RF power of the bias is 100 W, the running times for 400 nm and 630 nm samples are 30 s and 45 s, respectively. As a result, the metasurfaces are obtained after removing the residual aluminum with the stripping solution.

Phase object preparation

Phase plates were fabricated through the following procedure. First, a layer of photoresist (AZ1500) was spin-coated onto a silica substrate. Subsequently, specific target patterns were defined on the substrate via laser writing (Raith PicoMaster 100). Following this, silicon dioxide films with varying thicknesses were deposited using electron beam evaporation. Finally, a lift-off process was performed by ultrasonically treating the coated substrate in acetone, which removed the residual photoresist along with the overlying film, thereby successfully transferring the desired silicon oxide patterns onto the substrate.

Cell preparation

Human osteosarcoma U2OS cells were purchased from the American Type Culture Collection (ATCC). Cells were cultured in McCoy's 5 A medium (Gibco, Thermo Fisher Scientific; cat. no. 16600-082) supplemented with 10% (v/v) fetal bovine serum (FBS; Thermo Fisher Scientific; cat. no. A5669701) at 37 °C in a humidified 5% CO₂ incubator (Thermo Fisher Scientific). Cells were passaged three times weekly using 0.25% trypsin-EDTA (Gibco, Thermo Fisher Scientific; cat. no. 25200-072). One day prior to experiments, cells were seeded onto 35-mm glass-bottom μ -Dishes (ibidi; cat. no. 81158) and imaged after allowing sufficient time for cell attachment and spreading.

Data availability

All data supporting the findings of this study are available within the paper and its Supplementary Information.

Received: 31 December 2025; Accepted: 21 March 2026;

Published online: 13 April 2026

References

- Park, Y., Depeursing, C. & Popescu, G. Quantitative phase imaging in biomedicine. *Nat. Photonics* **12**, 578–589 (2018).
- Atkinson, G. A. & Hancock, E. R. Recovery of surface orientation from diffuse polarization. *IEEE Trans. Image Process.* **15**, 1653–1664 (2006).
- Arwin, H. et al. Optical chirality determined from mueller matrices. *Appl. Sci.* **11**, 6742 (2021).
- He, C. et al. Polarisation optics for biomedical and clinical applications: a review. *Light Sci. Appl.* **10**, 194 (2021).
- Losurdo, M. et al. Spectroscopic ellipsometry and polarimetry for materials and systems analysis at the nanometer scale: state-of-the-art, potential, and perspectives. *J. Nanopart. Res.* **11**, 1521–1554 (2009).
- Tyo, J. S., Goldstein, D. L., Chenault, D. B. & Shaw, J. A. Review of passive imaging polarimetry for remote sensing applications. *Appl. Opt.* **45**, 5453 (2006).
- Cai, L. Z., Liu, Q. & Yang, X. L. Phase-shift extraction and wave-front reconstruction in phase-shifting interferometry with arbitrary phase steps. *Opt. Lett.* **28**, 1808 (2003).
- Gao, P., Harder, I., Nercissian, V., Mantel, K. & Yao, B. Phase-shifting point-diffraction interferometry with common-path and in-line configuration for microscopy. *Opt. Lett.* **35**, 712 (2010).
- Flores Muñoz, V. H. et al. Measurement of mean thickness of transparent samples using simultaneous phase shifting interferometry with four interferograms. *Appl. Opt.* **55**, 4047 (2016).
- Varghese, A., Das, B. & Singh, R. K. Highly stable lens-less digital holography using cyclic lateral shearing interferometer and residual decollimated beam. *Opt. Commun.* **422**, 3–7 (2018).
- Tiwari, V. & Khodadad, D. Self-referenced polarization augmented Jones matrix imaging using cyclic shearing interferometry. *Opt. Lett.* **51**, 929 (2026).
- Zuo, C. et al. Transport of intensity equation: a tutorial. *Opt. Lasers Eng.* **135**, 106187 (2020).
- Zhang, J., Chen, Q., Sun, J., Tian, L. & Zuo, C. On a universal solution to the transport-of-intensity equation. *Opt. Lett.* **45**, 3649 (2020).
- Zuo, C., Chen, Q., Yu, Y. & Asundi, A. Transport-of-intensity phase imaging using Savitzky-Golay differentiation filter - theory and applications. *Opt. Express* **21**, 5346 (2013).
- Berry, H. G., Gabrielse, G. & Livingston, A. E. Measurement of the Stokes parameters of light. *Appl. Opt.* **16**, 3200 (1977).
- Baek, N., Lee, Y., Kim, T., Jung, J. & Lee, S. A. Lensless polarization camera for single-shot full-Stokes imaging. *APL Photonics* **7**, 116107 (2022).
- Petrini, A., Conti, C. & Pierangeli, D. Single-shot full-stokes analysis of partially-polarized light with a photonic deep random neural network. *Laser Photonics Rev.* e01467 <https://doi.org/10.1002/lpor.202501467> (2025).
- Khorasaninejad, M. et al. Metalenses at visible wavelengths: Diffraction-limited focusing and subwavelength resolution imaging. *Science* **352**, 1190–1194 (2016).
- Khorasaninejad, M. & Capasso, F. Metalenses: versatile multifunctional photonic components. *Science* **358**, eaam8100 (2017).
- Wang, S. et al. Arbitrary polarization conversion dichroism metasurfaces for all-in-one full Poincaré sphere polarizers. *Light Sci. Appl.* **10**, 24 (2021).
- Tseng, E. et al. Neural nano-optics for high-quality thin lens imaging. *Nat. Commun.* **12**, 6493 (2021).
- Dong, Y. et al. Achromatic single metalens imaging via deep neural network. *ACS Photonics* <https://doi.org/10.1021/acsp Photonics.3c01870> (2024).
- Fan, Q. et al. Trilobite-inspired neural nanophotonic light-field camera with extreme depth-of-field. *Nat. Commun.* **13**, 2130 (2022).
- Shen, Z. et al. Monocular metasurface camera for passive single-shot 4D imaging. *Nat. Commun.* **14**, 1035 (2023).
- Fu, B. et al. Miniaturized high-efficiency snapshot polarimetric stereoscopic imaging. *Optica* **12**, 391 (2025).
- Zaidi, A. et al. Metasurface-enabled single-shot and complete Mueller matrix imaging. *Nat. Photonics* <https://doi.org/10.1038/s41566-024-01426-x> (2024).
- Zhang, Q. et al. Neural-optic co-designed polarization-multiplexed metalens for compact computational spectral imaging. *Laser Photonics Rev.* 2400187 <https://doi.org/10.1002/lpor.202400187> (2024).
- Li, L. et al. Single-shot deterministic complex amplitude imaging with a single-layer metalens. *Sci. Adv.* **10**, eadl0501 (2024).
- Hu, X. et al. Metasurface-based computational imaging: a review. *Adv. Photonics* **6**, (2024).
- Fröch, J. E. et al. Computational imaging with meta-optics. *Optica* **12**, 774 (2025).

31. Zhou, J. et al. Eagle-eye inspired meta-device for phase imaging. *Adv. Mater.* 2402751 <https://doi.org/10.1002/adma.202402751> (2024).
32. Min, Q. et al. Varifocal metalens for compact and accurate quantitative phase imaging. *ACS Photonics* <https://doi.org/10.1021/acsp Photonics.4c00658> (2024).
33. Engay, E., Huo, D., Malureanu, R., Bunea, A.-I. & Lavrinenko, A. Polarization-dependent all-dielectric metasurface for single-shot quantitative phase imaging. *Nano Lett.* **21**, 3820–3826 (2021).
34. Wang, J. et al. Quantitative phase imaging with a compact meta-microscope. *npj Nanophoton.* **1**, 4 (2024).
35. Shanker, A. et al. Quantitative phase imaging endoscopy with a metalens. *Light Sci. Appl.* **13**, 305 (2024).
36. Zhou, J. et al. Advanced quantitative phase microscopy achieved with spatial multiplexing and a metasurface. *Nano Lett.* **25**, 2034–2040 (2025).
37. Cheng, J. et al. Tunable meta-device for large depth of field quantitative phase imaging. *Nanophotonics* <https://doi.org/10.1515/nanoph-2024-0661> (2025).
38. Rubin, N. A. et al. Matrix Fourier optics enables a compact full-Stokes polarization camera. *Science* **365**, eaax1839 (2019).
39. Fan, Q. et al. Disordered metasurface enabled single-shot full-Stokes polarization imaging leveraging weak dichroism. *Nat. Commun.* **14**, 7180 (2023).
40. Zuo, J. et al. Chip-integrated metasurface full-Stokes polarimetric imaging sensor. *Light Sci. Appl.* **12**, 218 (2023).
41. Wang, Y. et al. Non-interleaved shared-aperture full-stokes metalens via prior-knowledge-driven inverse design. *Adv. Mater.* **37**, 2408978 (2025).
42. Xia, H. et al. Inverse design of cascaded multidimensional coding metasurface for snapshot full-stokes imaging and depth estimation. *ACS Photonics* <https://doi.org/10.1021/acsp Photonics.5c02216> (2025).
43. Li, F.-J. et al. Meta-grating-lens-based monolithic polarization camera. *Sci. Adv.* **11**, eadx9886 (2025).
44. Bao, Y. & Li, B. Single-shot simultaneous intensity, phase and polarization imaging with metasurface. *Natl. Sci. Rev.* **12**, nwae418 (2025).
45. Kato, K., Hammar, K., Smith, P. J. S. & Oldenbourg, R. Birefringence imaging directly reveals architectural dynamics of filamentous actin in living growth cones. *MBoC* **10**, 197–210 (1999).

Acknowledgements

The work is supported by the Key Research and Development Program from Ministry of Science and Technology of China (2022YFA1205000), National Natural Science Foundation of China (12274217, 62305092), and Fundamental Research Funds for the Central Universities. The

microfabrication center of the National Laboratory of Solid-State Microstructures of Nanjing University is acknowledged for their technique support.

Author contributions

Q.Z. conceived the idea, performed the numerical simulations, and wrote the original draft. P.L. fabricated the metasurface sample. X.J. prepared the biological samples. L.L. and J.L. fabricated the phase plates. Q.Z., H.X., and C.Z. performed the experimental measurements. C.W., C.Y., and Y.H. assisted with data analysis and manuscript preparation. All authors contributed to the interpretation and analysis of results. T.X. and Z.Z. directed the project.

Competing interests

The authors declare no competing interests.

Additional information

Supplementary information The online version contains supplementary material available at <https://doi.org/10.1038/s44310-026-00122-8>.

Correspondence and requests for materials should be addressed to Ting Xu or Zhenrong Zheng.

Reprints and permissions information is available at <http://www.nature.com/reprints>

Publisher's note Springer Nature remains neutral with regard to jurisdictional claims in published maps and institutional affiliations.

Open Access This article is licensed under a Creative Commons Attribution-NonCommercial-NoDerivatives 4.0 International License, which permits any non-commercial use, sharing, distribution and reproduction in any medium or format, as long as you give appropriate credit to the original author(s) and the source, provide a link to the Creative Commons licence, and indicate if you modified the licensed material. You do not have permission under this licence to share adapted material derived from this article or parts of it. The images or other third party material in this article are included in the article's Creative Commons licence, unless indicated otherwise in a credit line to the material. If material is not included in the article's Creative Commons licence and your intended use is not permitted by statutory regulation or exceeds the permitted use, you will need to obtain permission directly from the copyright holder. To view a copy of this licence, visit <http://creativecommons.org/licenses/by-nc-nd/4.0/>.

© The Author(s) 2026